Science Advances
AAAS

advances.sciencemag.org/cgi/content/full/6/30/eabb7417/DC1

Supplementary Materials for

Geometrically reconfigurable 3D mesostructures and electromagnetic devices through a rational bottom-up design strategy

Ke Bai, Xu Cheng, Zhaoguo Xue, Honglie Song, Lei Sang, Fan Zhang, Fei Liu,
Xiang Luo, Wen Huang, Yonggang Huang, Yihui Zhang*

*Corresponding author. Email: yihuizhang@tsinghua.edu.cn

Published 22 July 2020, *Sci. Adv.* **6**, eabb7417 (2020)
DOI: 10.1126/sciadv.abb7417

The PDF file includes:

Figs. S1 to S33
Legends for movies S1 to S4

Other Supplementary Material for this manuscript includes the following:

(available at advances.sciencemag.org/cgi/content/full/6/30/eabb7417/DC1)

Movies S1 to S4

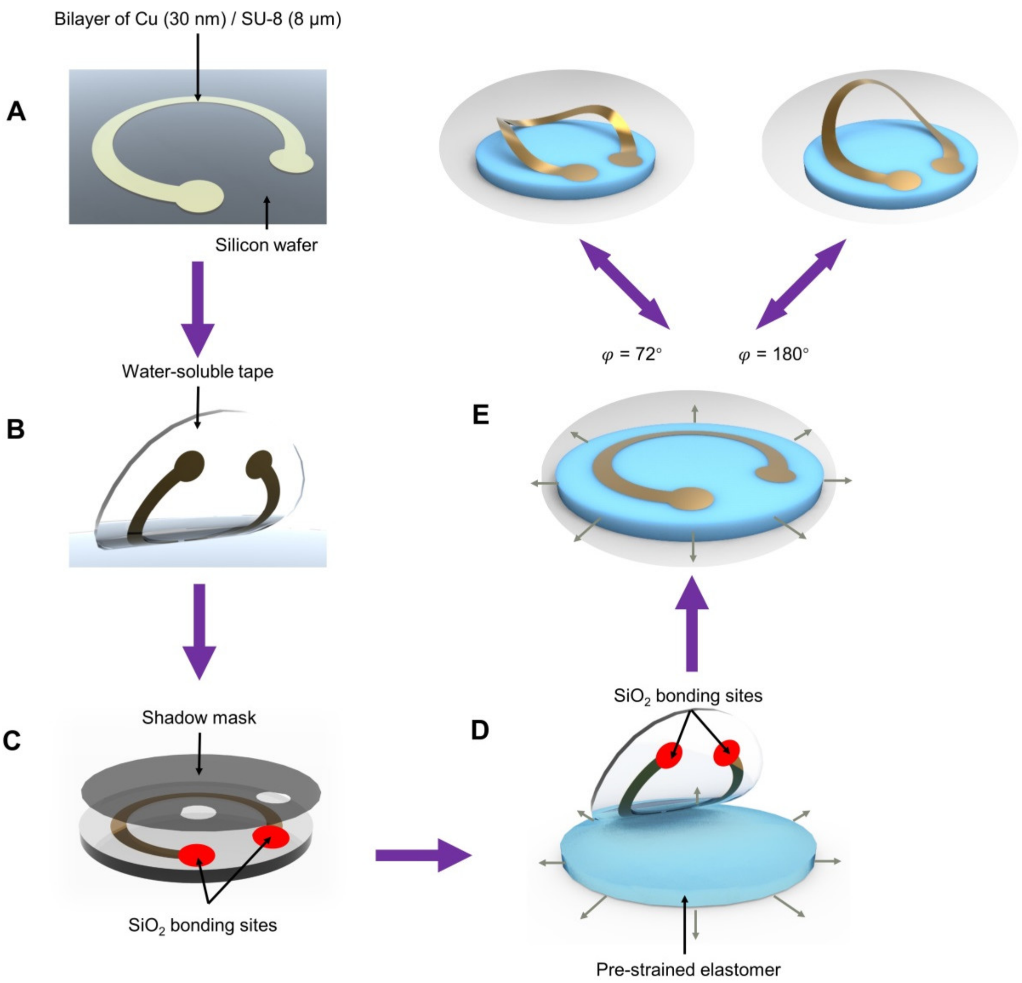

fig. S1. Photolithographic fabrication scheme for 3D reconfigurable mesostructures. (**A**), Pattern 2D precursor of a Cu/SU-8 bilayer on silicon substrate. (**B**), Pick the 2D precursor up with a water-soluble tape. (**C**), Layer of SiO_2 deposited by electron-beam evaporation through the shadow mask defined the bonding sites, followed by removal of the shadow mask. (**D**), Form a strong adhesion between SiO_2 bonding sites and elastomer through the UV-light exposure, followed by dissolution of water-soluble tape. (**E**), Release the pre-stretched elastomer along different paths to realize distinct stable 3D configurations.

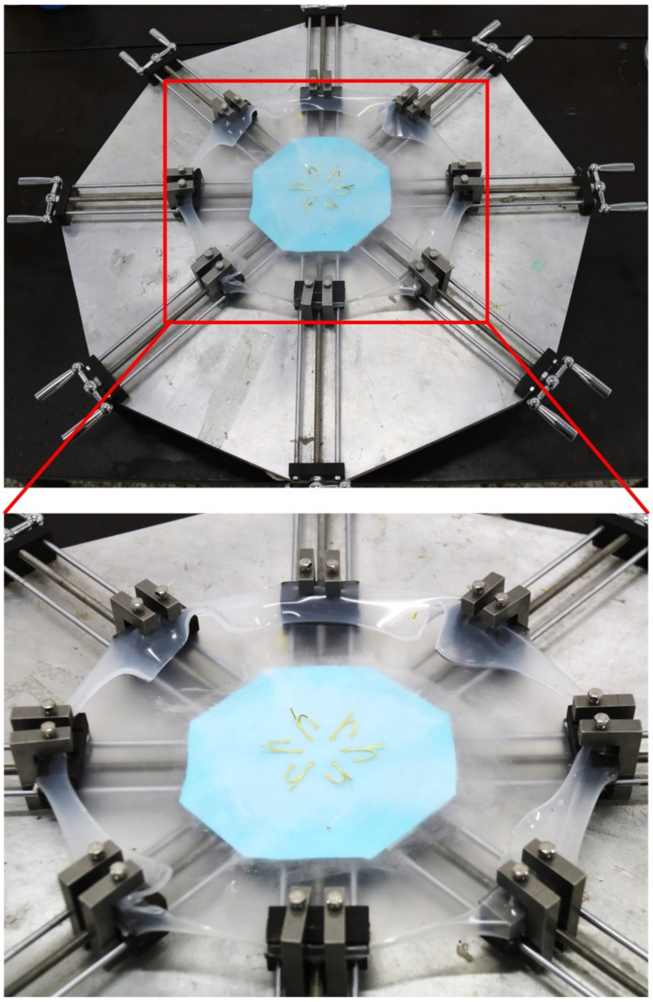

fig. S2. Optical images of a pre-stretched elastomer substrate loaded using a four-axis stretcher. Photo Credit: Ke Bai, Tsinghua University.

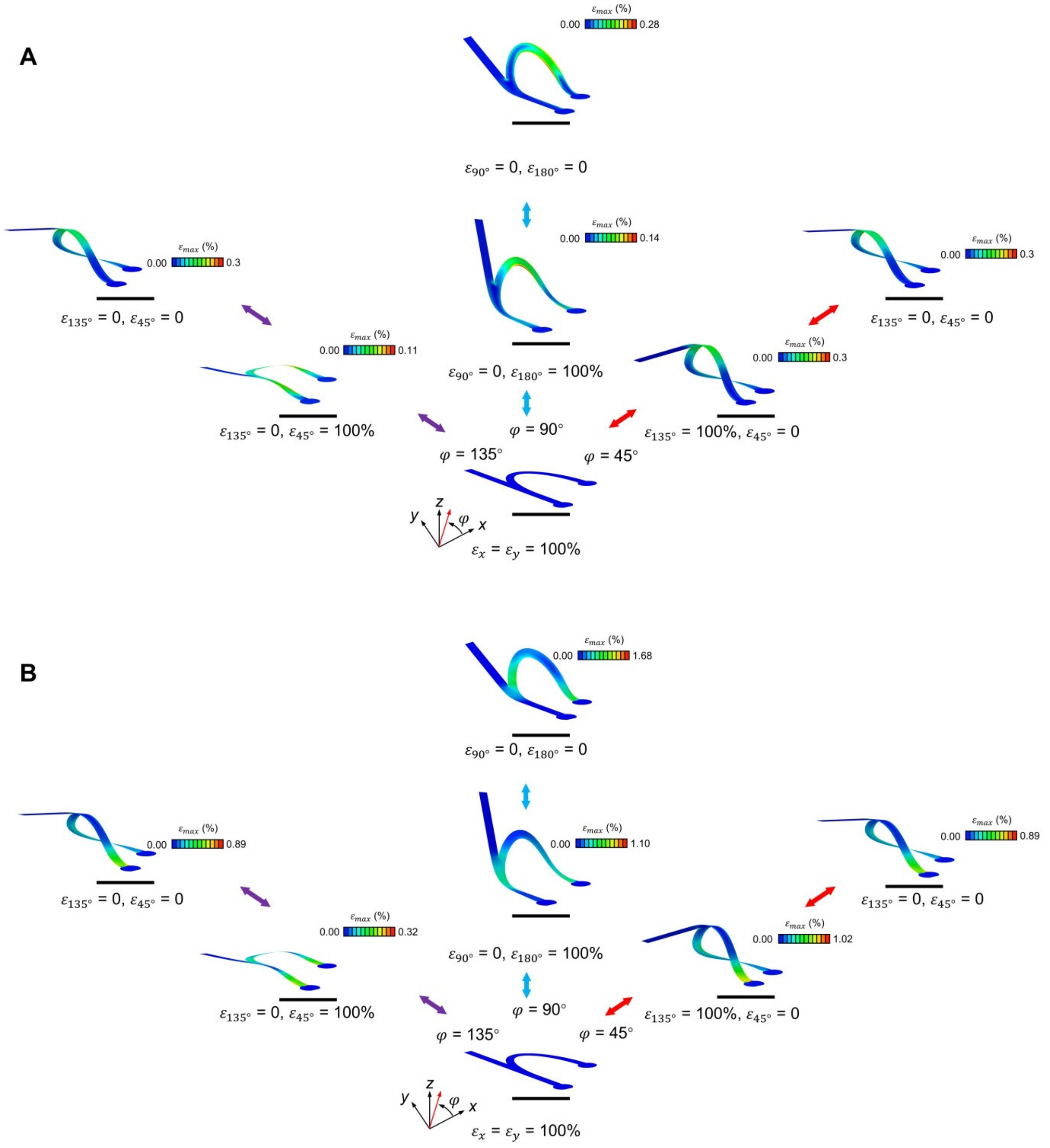

fig. S3. Distributions of the maximum principal strain in a 3D ribbon mesostructure (corresponding to Fig. 1A) during the reconfiguration process. The colour denotes the magnitude of maximum principal strain in the aluminum layer (A) and PI layer (B). Scale bars, 5 mm.

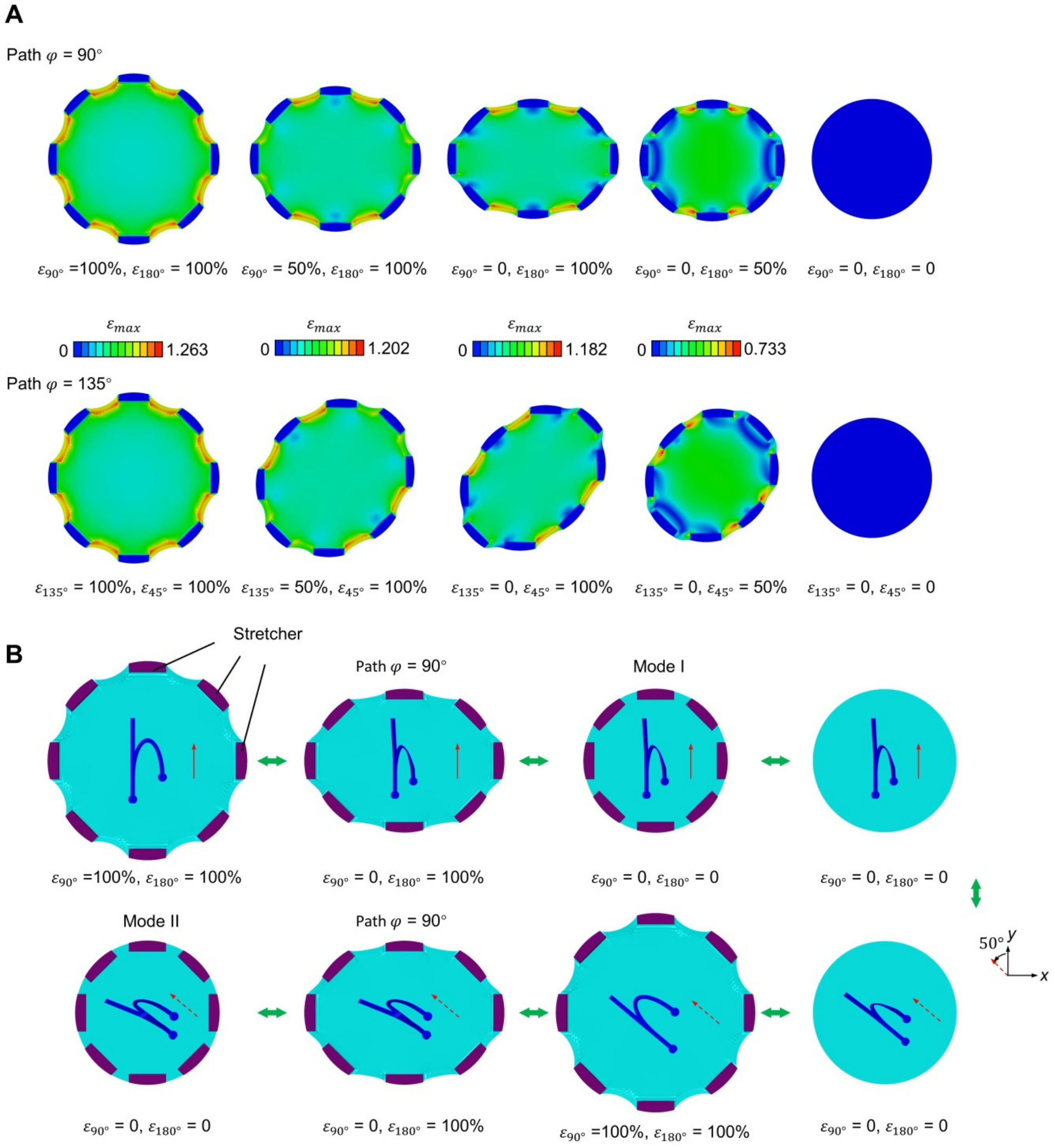

fig. S4. Distribution of the maximum principal strain in the elastomer substrate during the release process along two different angles (A) and schematic of process to obtain a different stable 3D configuration through rotation of the substrate to realize an arbitrary sequential release direction (B).

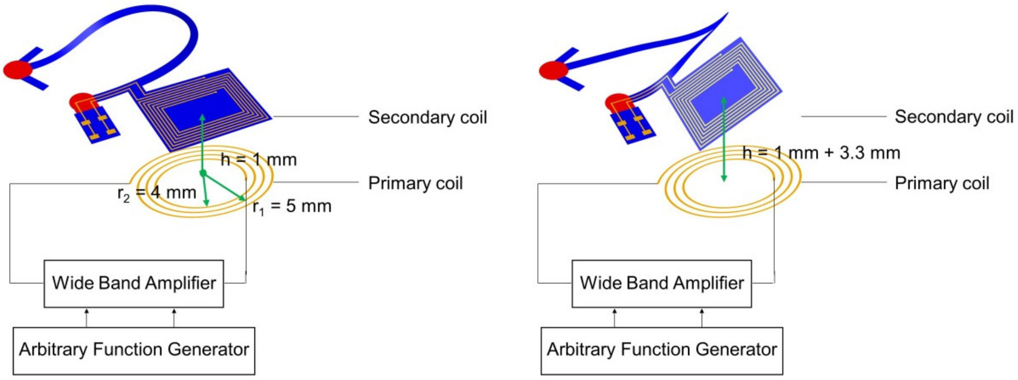

fig. S5. Schematic of the coil antenna at two different operation modes. The distance and angle between the primary coil and secondary coil in the two modes have a significant influence on the induced voltage in the secondary coil. According to the magnetic distribution model of the circular primary coil, the induced voltage can be estimated quantitatively (see the results in Fig. 1E).

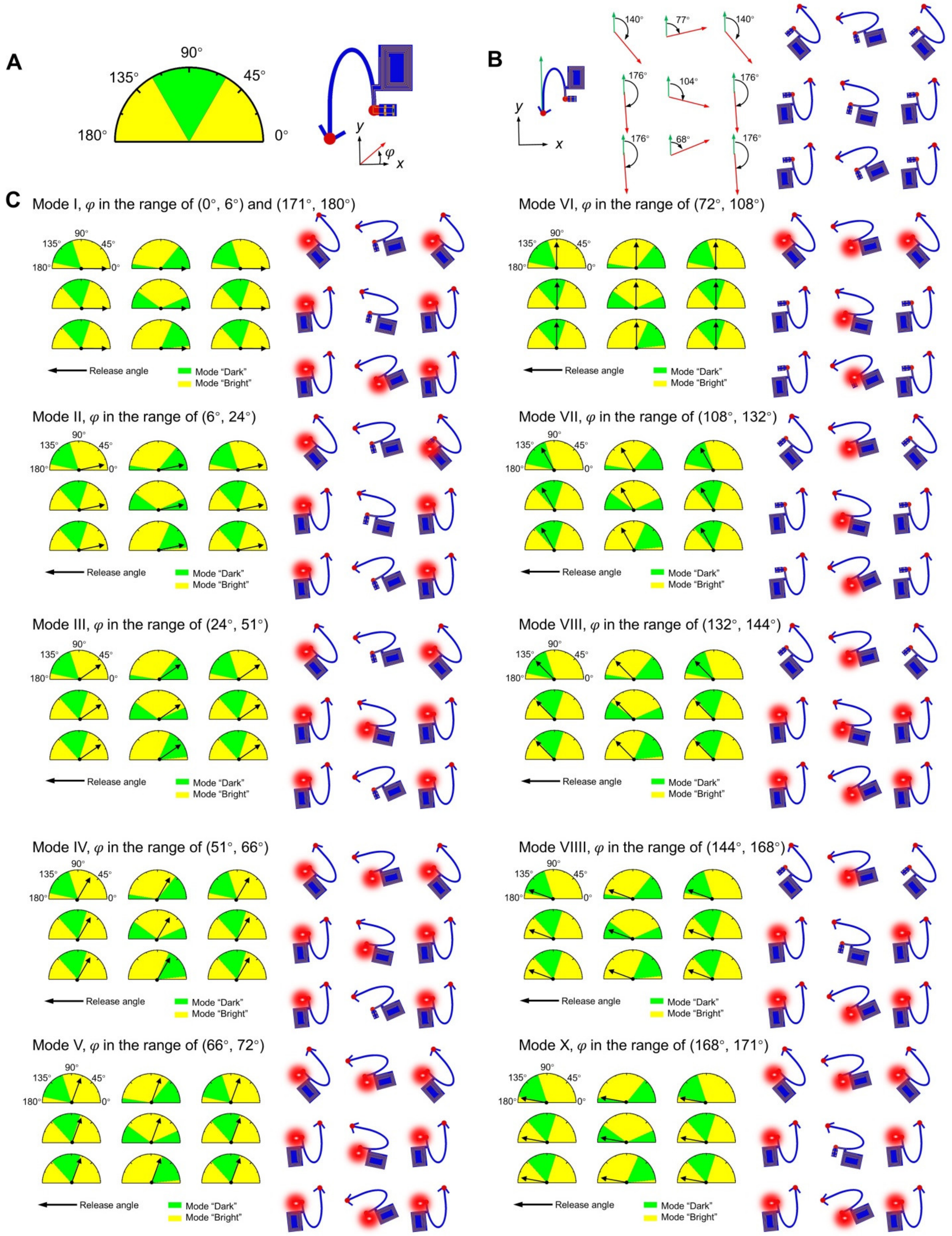

Mode I, φ in the range of (0°, 6°) and (171°, 180°)

Mode II, φ in the range of (6°, 24°)

Mode III, φ in the range of (24°, 51°)

Mode IV, φ in the range of (51°, 66°)

Mode V, φ in the range of (66°, 72°)

Mode VI, φ in the range of (72°, 108°)

Mode VII, φ in the range of (108°, 132°)

Mode VIII, φ in the range of (132°, 144°)

Mode VIIII, φ in the range of (144°, 168°)

Mode X, φ in the range of (168°, 171°)

fig. S6. Ten different operation modes of the antenna array. (A), The phase diagram of a single coil antenna. **(B)**, optimizing the direction of each coil antenna in the array to obtain target working modes. **(C)**, All of the ten possible different operation modes, along with the phase diagrams.

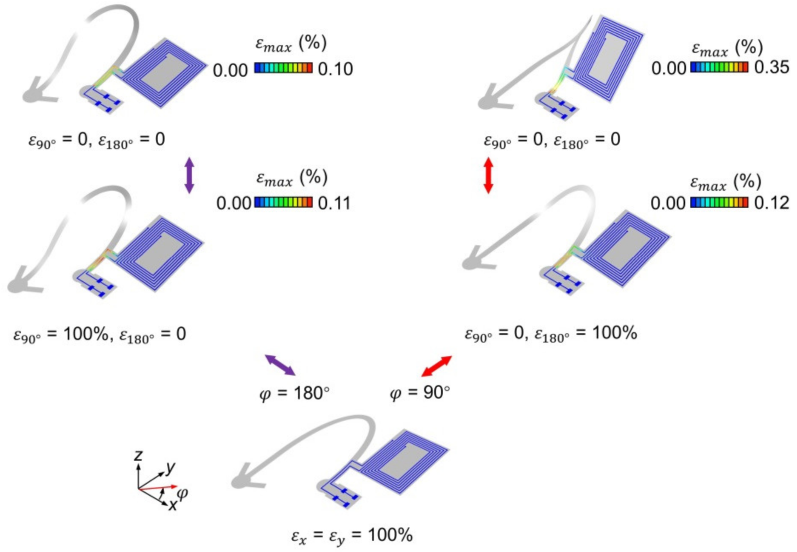

fig. S7. Distribution of principal strain of the coil antenna during the reconfiguration process. The colour in the FEA results corresponds to the magnitude of maximum principal strain in the copper layer.

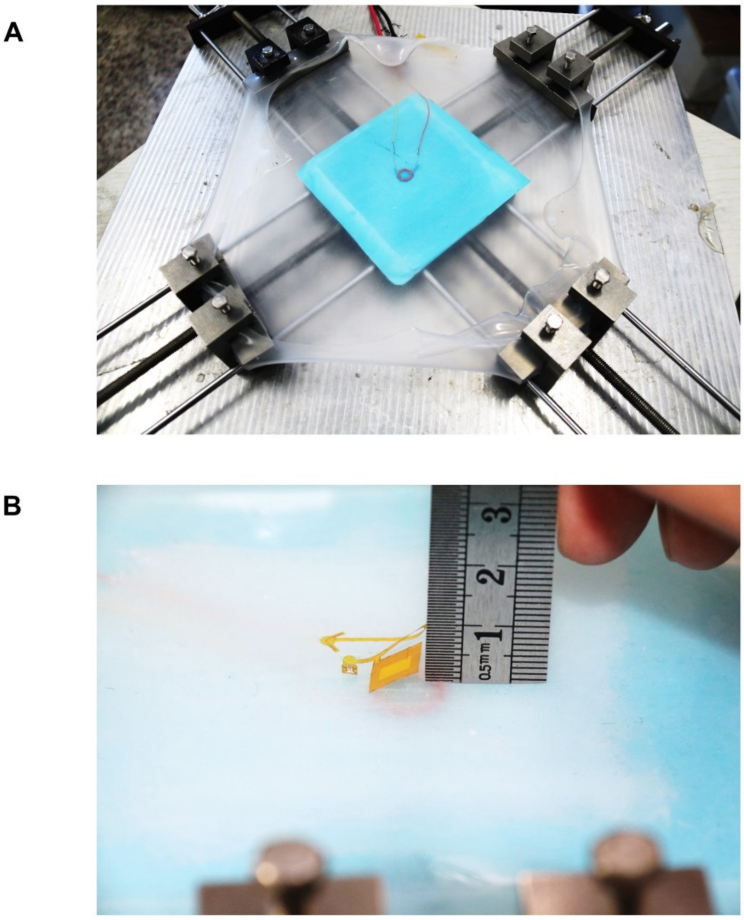

fig. S8. Illustration of mechanical stage and measurement during the cyclic test. (A), Optical image of a four-axis stretcher used for cycling test. **(B)**, Optical image of the measurement of the out-of-plane displacement of the secondary coil in the antenna. Photo Credit: Ke Bai, Tsinghua University.

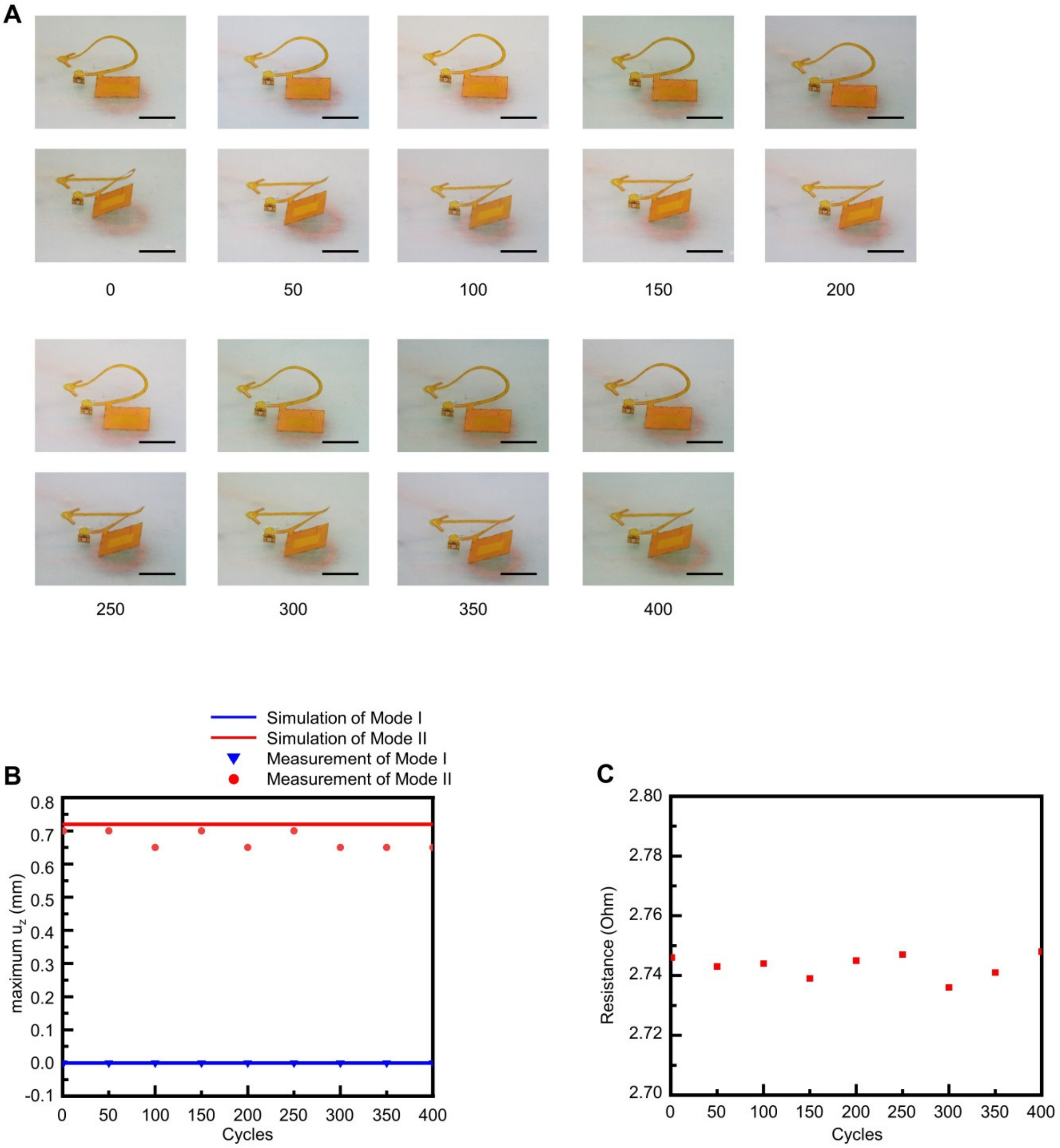

fig. S9. Results of deformation and electrical resistance during the cyclic test. **(A)**, Optical images of the coil antenna during the cyclic testing of the device in Fig. 1C, and with an amplitude = 50% (ε_{pre} = 100%) and a strain rate of ~ 0.03 s^{-1}. **(B-C)**, Maximum out-of-plane displacement of the secondary coil in the antenna (B) and resistance (C) of the circuit versus cycles of the testing. Scale bars, 5 mm. Photo Credit: Ke Bai, Tsinghua University.

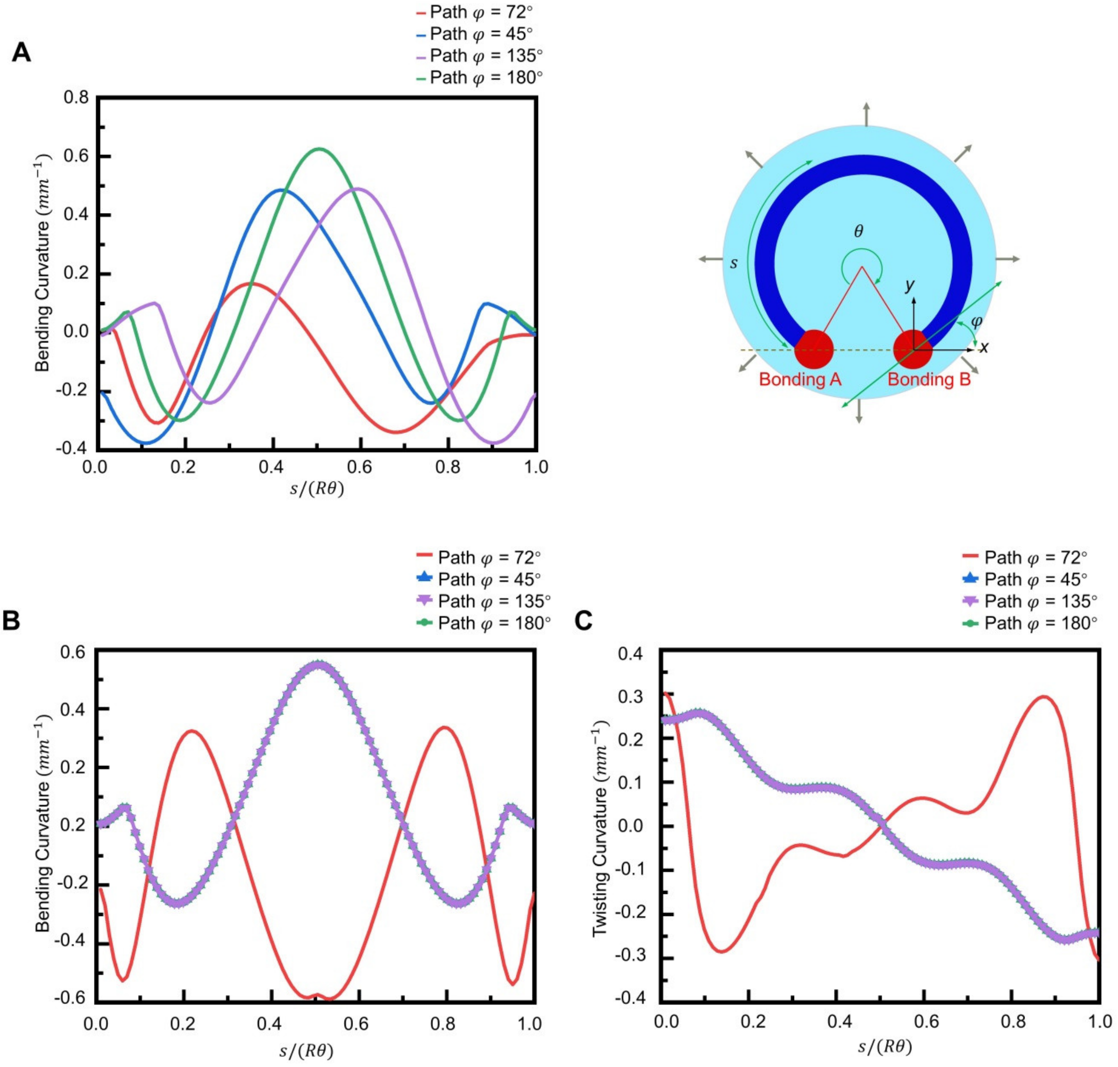

fig. S10. Distributions of curvature components during the sequential loading process along four different paths. (A), Distributions of bending curvatures with respect to the normalized arc-length coordinate of the ribbon precursor ($\theta = 1.7\pi$), after the first step of prestrain release for four different release angles (φ = 72°, 45°, 135° and 180°). **(B-C)**, Distribution of bending curvatures (B) and twisting curvatures (C) after the second step of prestrain release for four different release angles (φ = 72°, 45°, 135° and 180°). In b and c, the curves (φ = 45°, 135° and 180°) corresponding to the same stable 3D configuration overlap with each other.

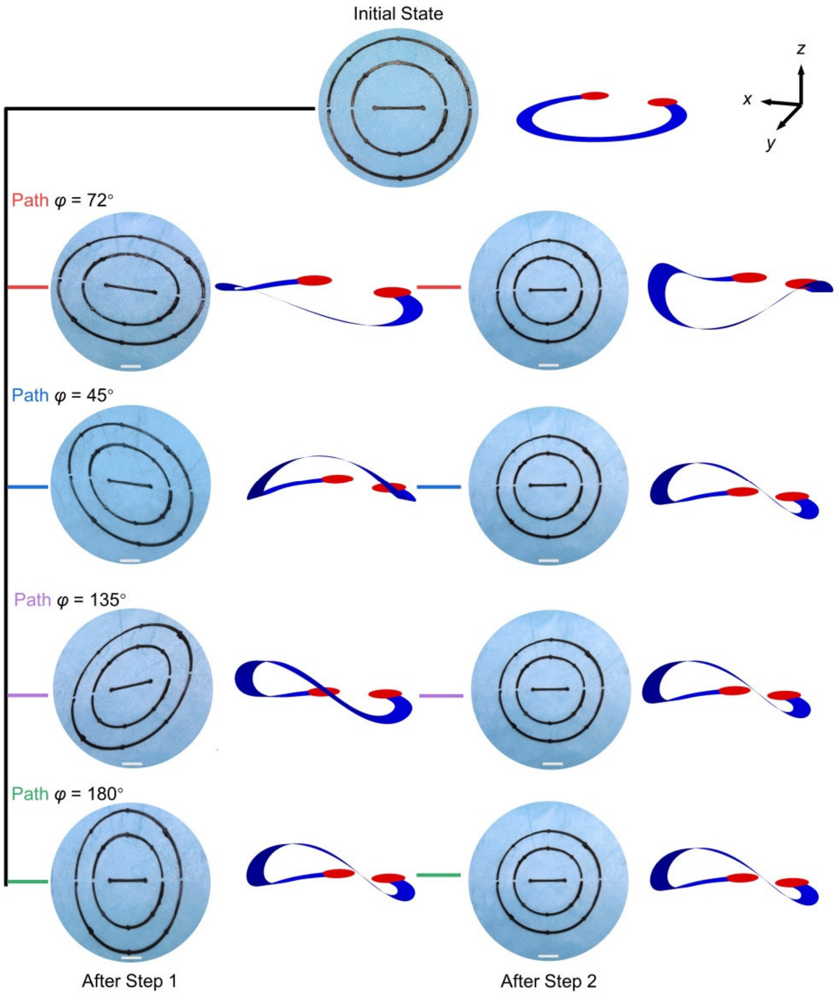

fig. S11. Shape transformation of the elastomer substrate and the corresponding mesostructure deformations during the sequential loading process along four different paths. The circular lines on the substrate that serve as a marker are generated using carbon paste. Scale bars, 5 mm. Photo Credit: Ke Bai, Tsinghua University.

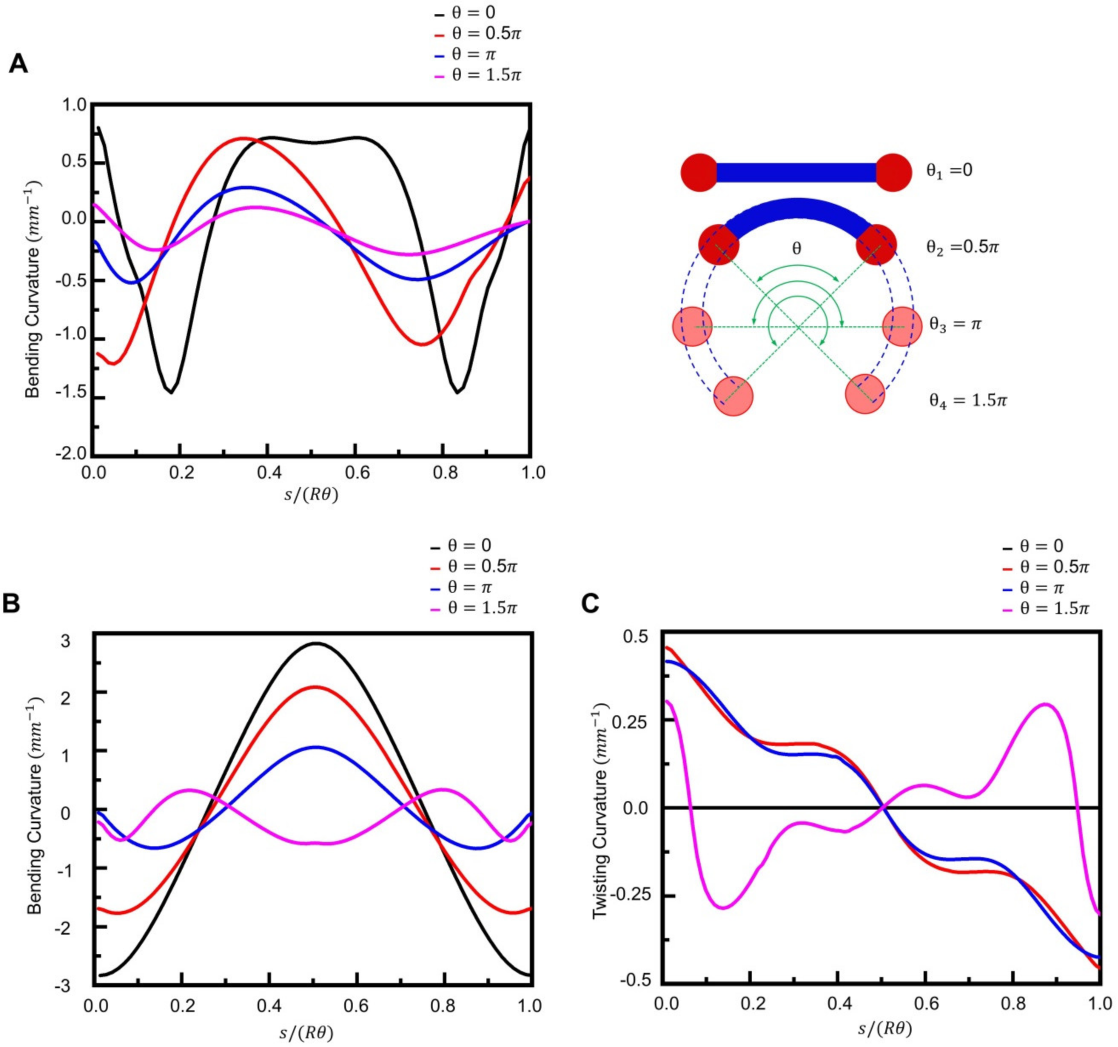

fig. S12. Distributions of curvature components during the sequential loading process along four different geometries. (A), Distributions of bending curvatures with respect to the normalized arc-length coordinate of the ribbon precursor, after the first step of prestrain release for arc ribbons with four different central angles (θ = 0, 0.5π, π and 1.5π). **(B-C),** Distributions of bending curvatures (B) and twisting curvatures (C) after the second step of prestrain release. Here, the release angle is fixed at φ = 72°.

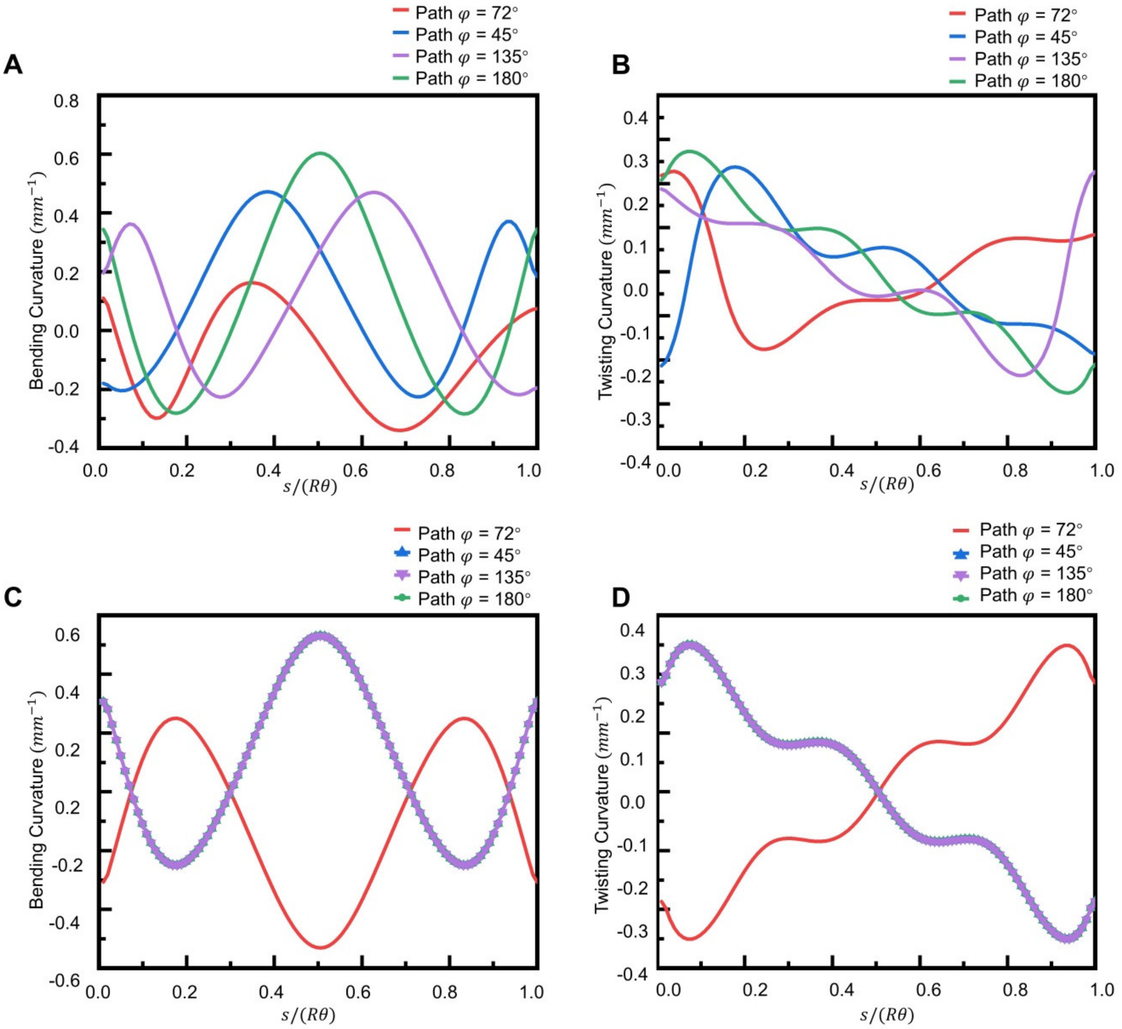

fig. S13. Distributions of curvature components without consideration of the mechanical interaction of supporting substrate. (A-B), Distributions of bending curvatures (A) and twisting curvatures (B) with respect to the normalized arc-length coordinate of the ribbon precursor ($\theta = 1.7\pi$), after the first step of prestrain release for four different release angles (φ = 72°, 45°, 135° and 180°). **(C-D),** Similar results of curvature distributions after the second step of prestrain release. In (C) and (D), the curves (φ = 45°, 135° and 180°) corresponding to the same stable 3D configuration overlap with each other

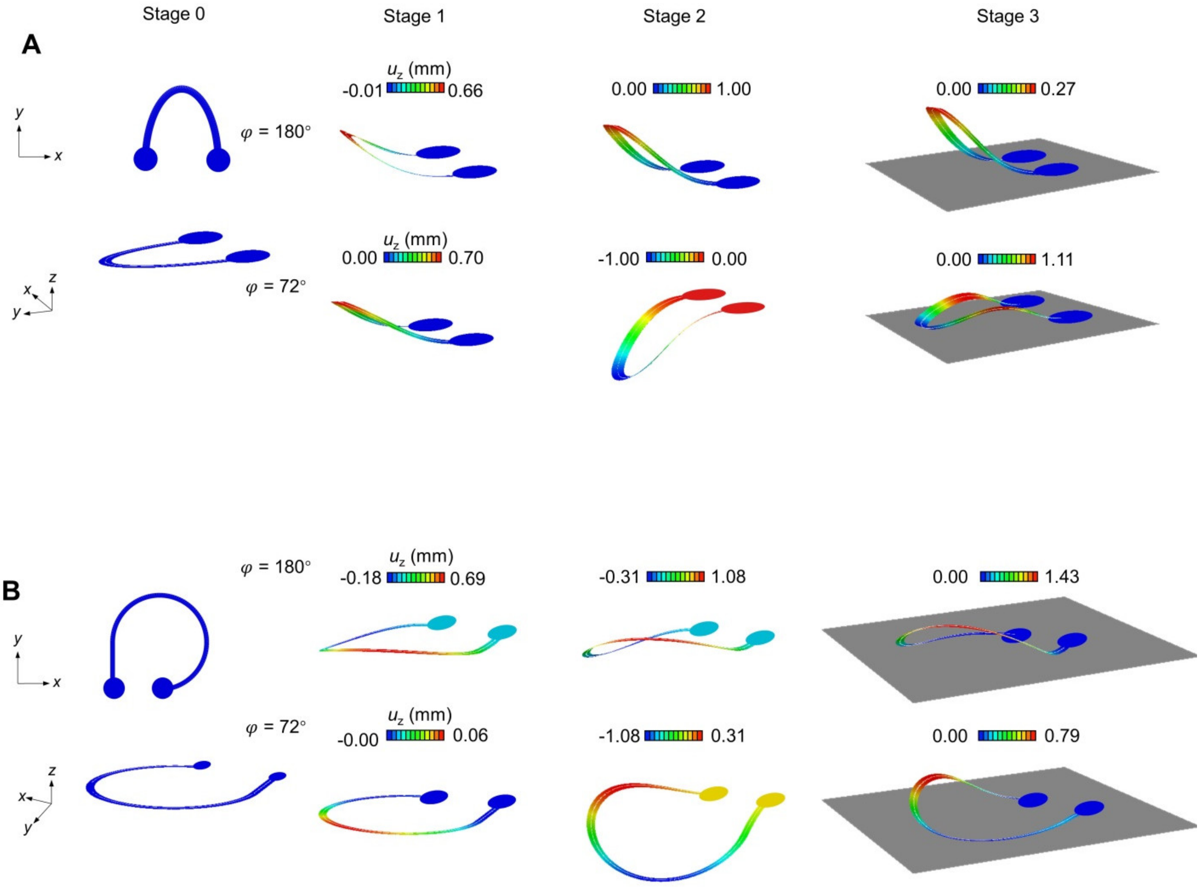

fig. S14. Additional examples that illustrate the physical mechanism of symmetry break induced by the supporting substrate. The 2D precursor consists of a symmetric elliptic ribbon in (A) and a combination of an arc ribbon and a straight ribbon in (B).

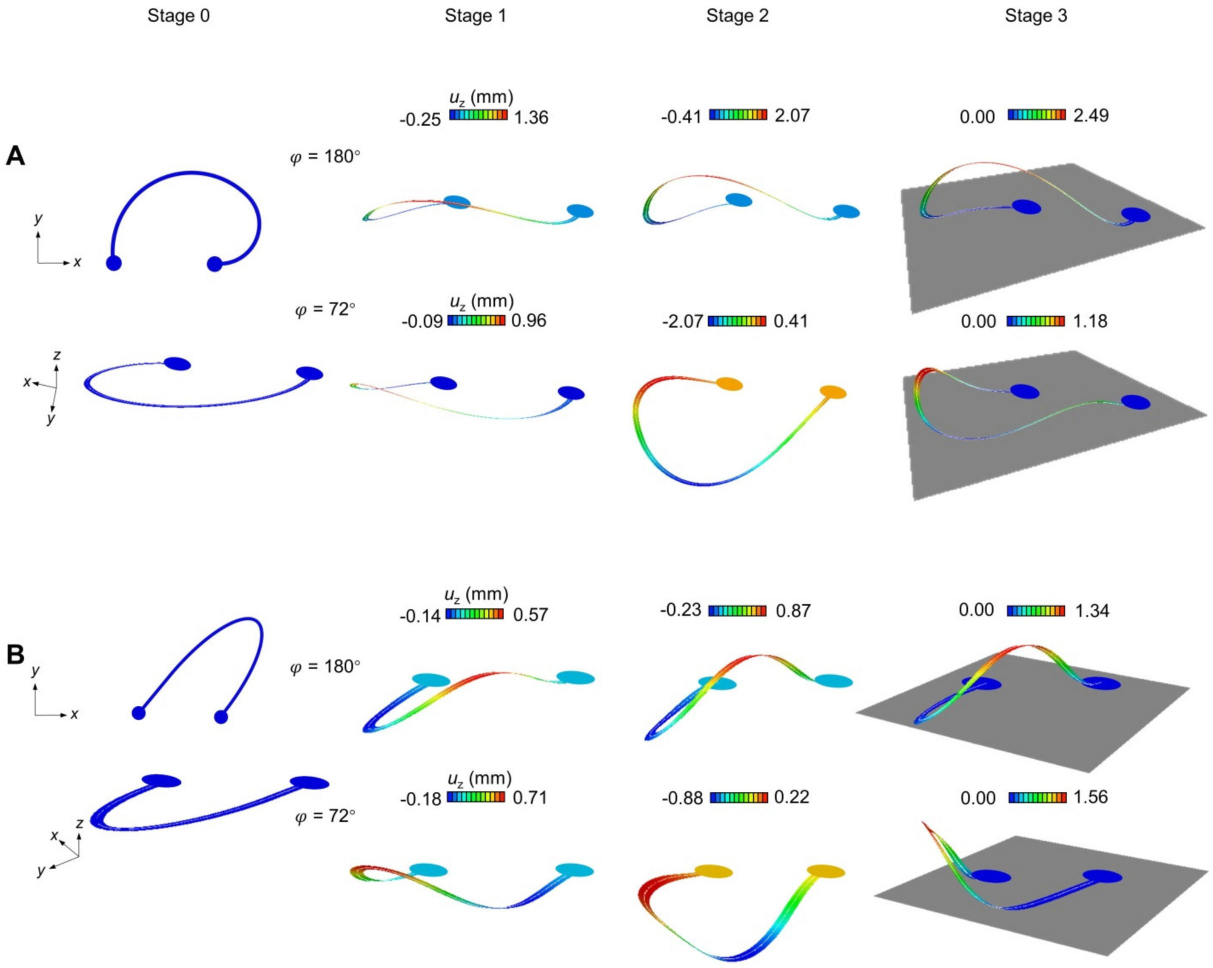

fig. S15. Additional examples that illustrate the physical mechanism of symmetry break induced by the supporting substrate. The 2D precursor consists of two arc ribbons in (A) and a combination of a semi-ellipse ribbon and a straight ribbon in (B).

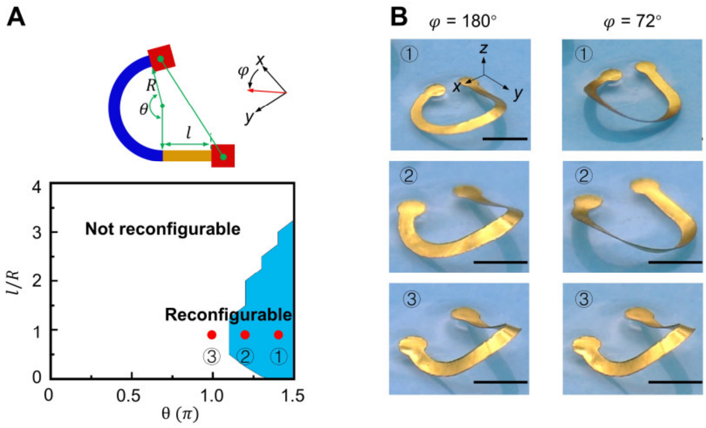

fig. S16. Design map of the reconfigurability for the 2D precursor consisting of an arc ribbon, and a straight ribbon and optical images at 3 representative cases. (A), Design map of the reconfigurability for the 2D precursor consisting of an arc ribbon (central angle *θ* and radius *R*) and a straight ribbon (length *l*). **(B),** Optical images of the assembled mesostructures for three representative design points (①, ② and ③) marked in (A). Scale bars, 5 mm. Photo Credit: Ke Bai, Tsinghua University.

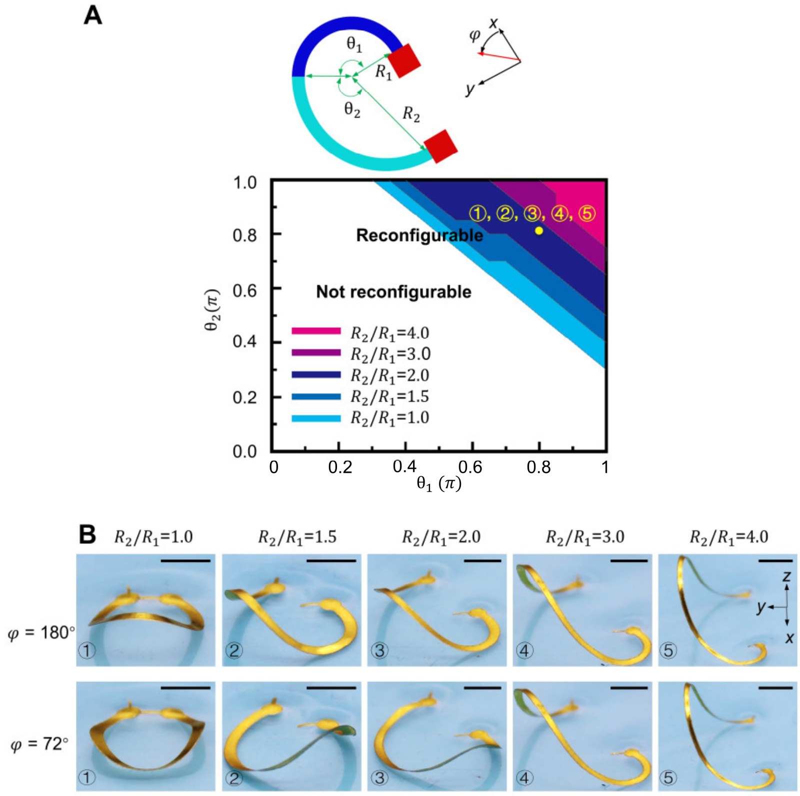

fig. S17. Design map of the reconfigurability for the 2D precursor consisting of two arc ribbons with different central angles and radii, and optical images at 5 representative cases. (A), Design map of the reconfigurability for the 2D precursor consisting of two arc ribbons with different central angles and radii. **(B)**, Optical images of the assembled mesostructures for five representative design points (① - ⑤) as marked in **(A)**. Scale bars, 5 mm. Photo Credit: Ke Bai, Tsinghua University.

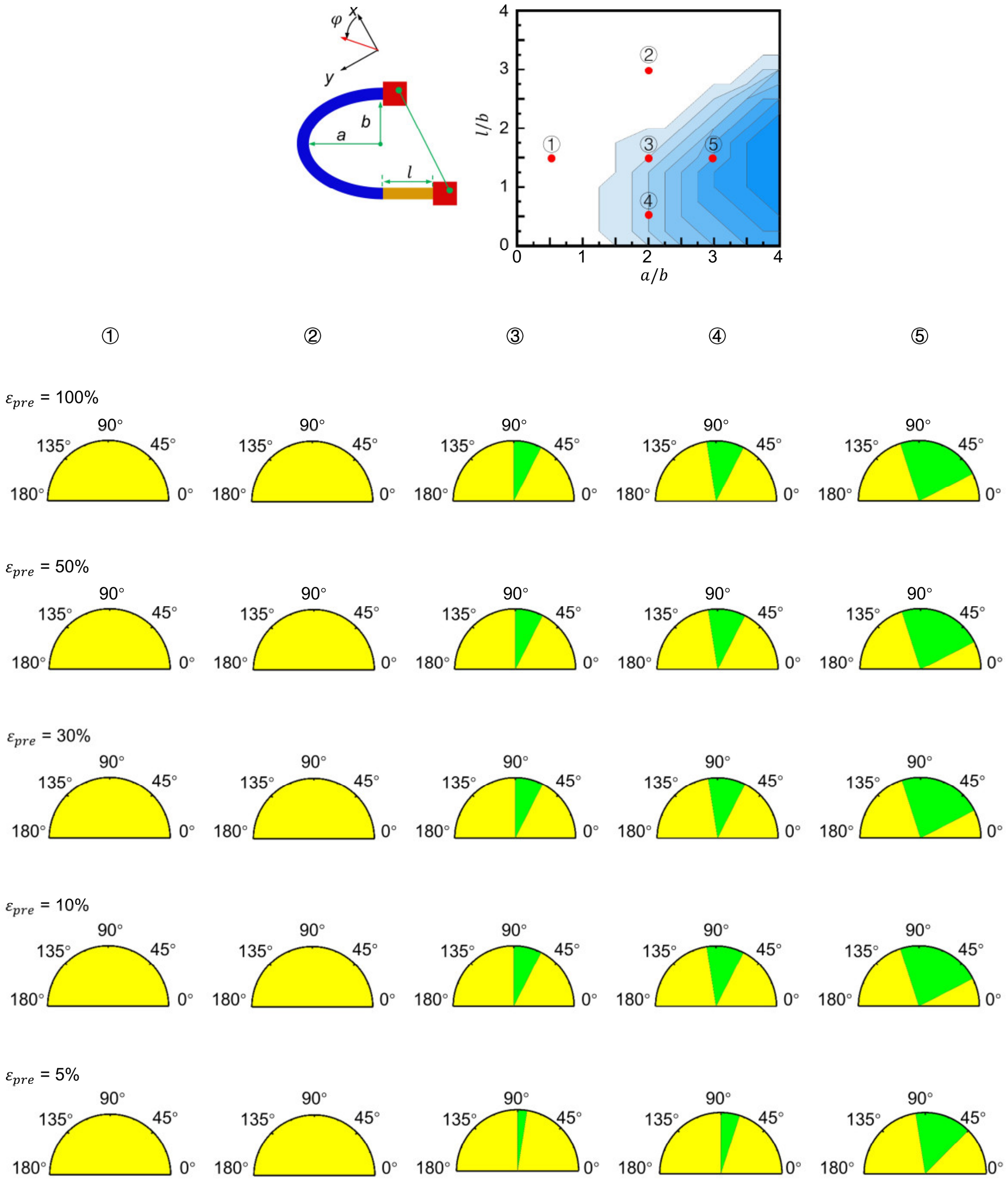

fig. S18. Influences of the magnitude of substrate prestrain on the reconfigurability of 3D mesostructures. Phase diagrams of the 2D precursors consisting of a semi-ellipse segment and a straight segment, with $\varepsilon_{\mathrm{pre}}$ set at 100%, 50%, 30%, 10% and 5%. Five design points marked in top panel are taken into account.

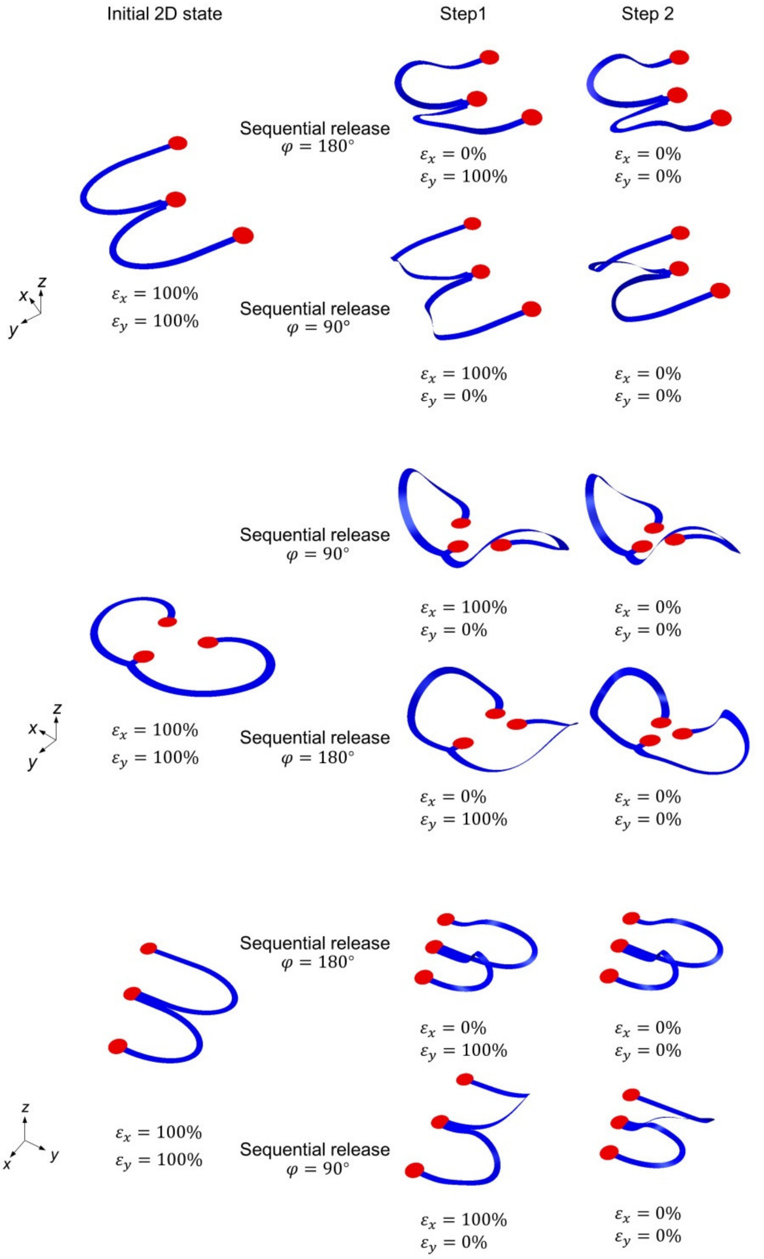

fig. S19. Deformation sequences for the ribbon-shaped 3D mesostructures in Fig. 3A along different release paths.

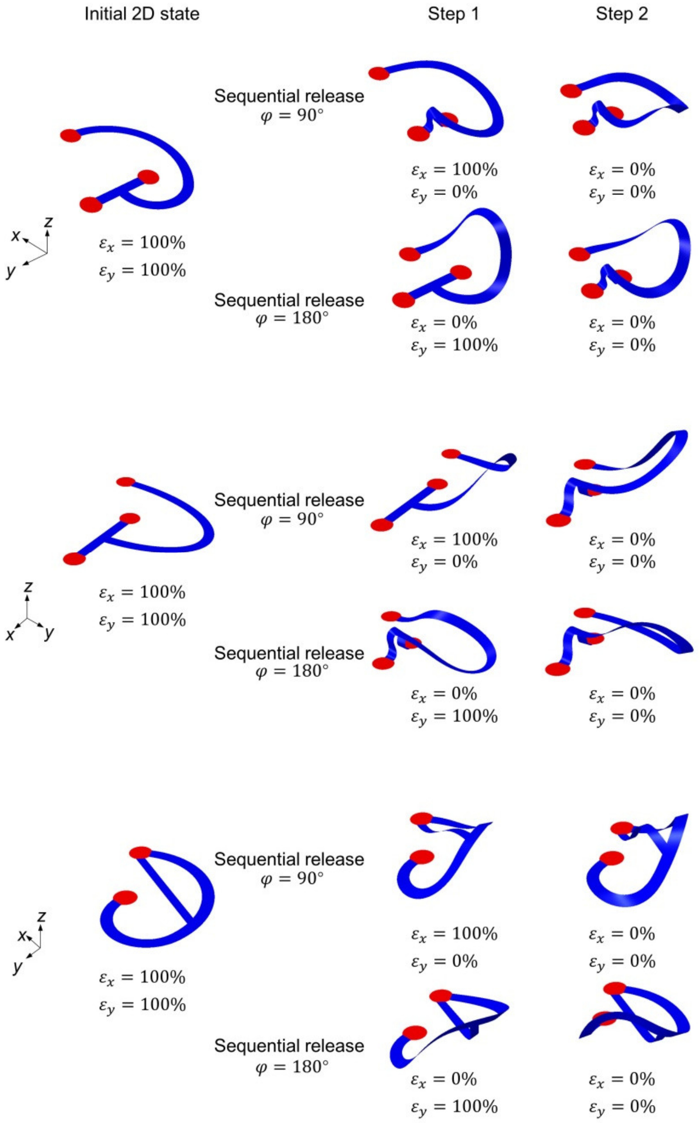

fig. S20. Deformation sequences for the ribbon-shaped 3D mesostructures in Fig. 3B along different release paths.

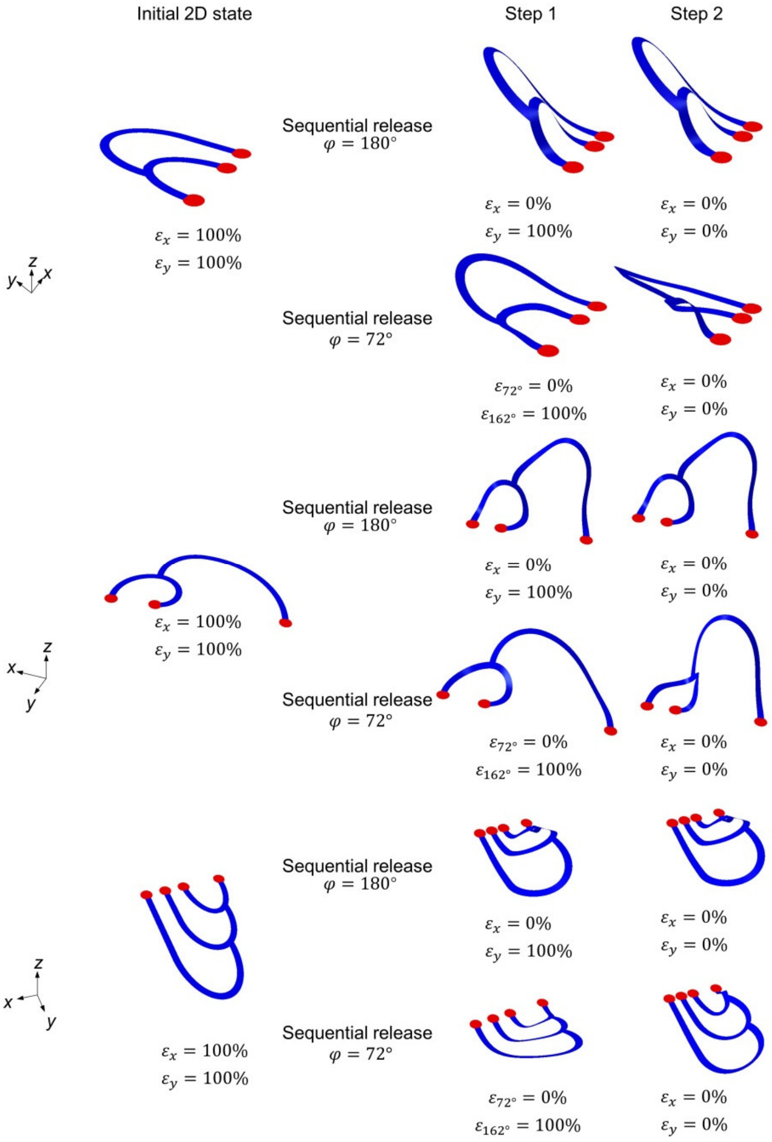

fig. S21. Deformation sequences for the ribbon-shaped 3D mesostructures in Fig. 3C along different release paths.

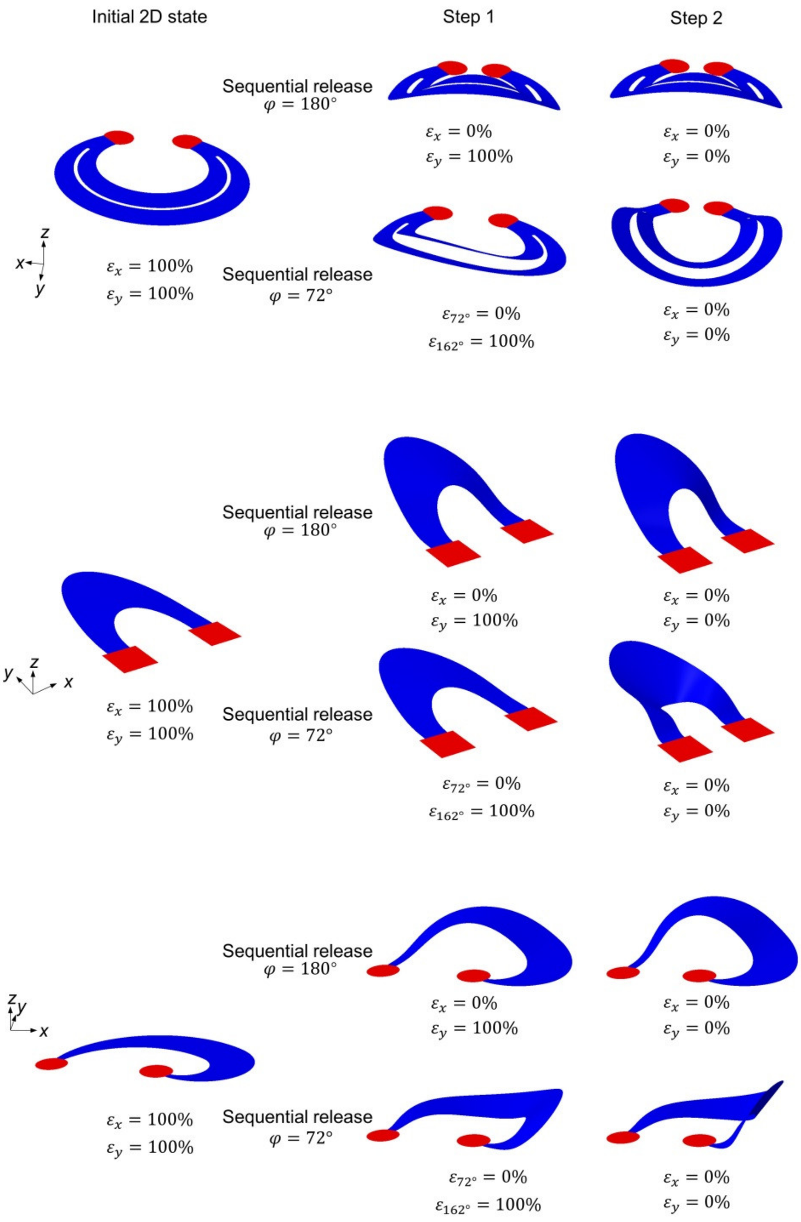

fig. S22. Deformation sequences for the membrane-shaped 3D mesostructures in Fig. 3D along different release paths.

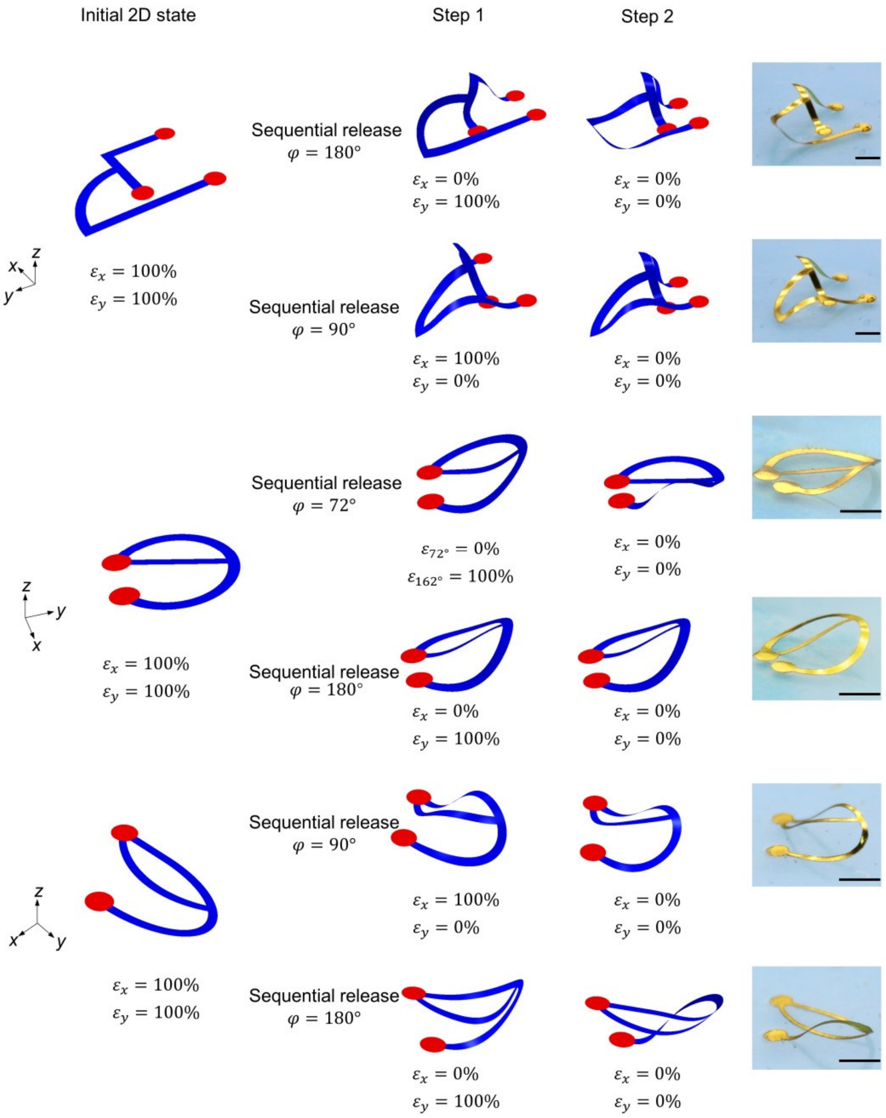

fig. S23. Additional examples of reconfigurable 3D mesostructures and the associated deformation sequences along different release paths. Photo Credit: Ke Bai, Tsinghua University.

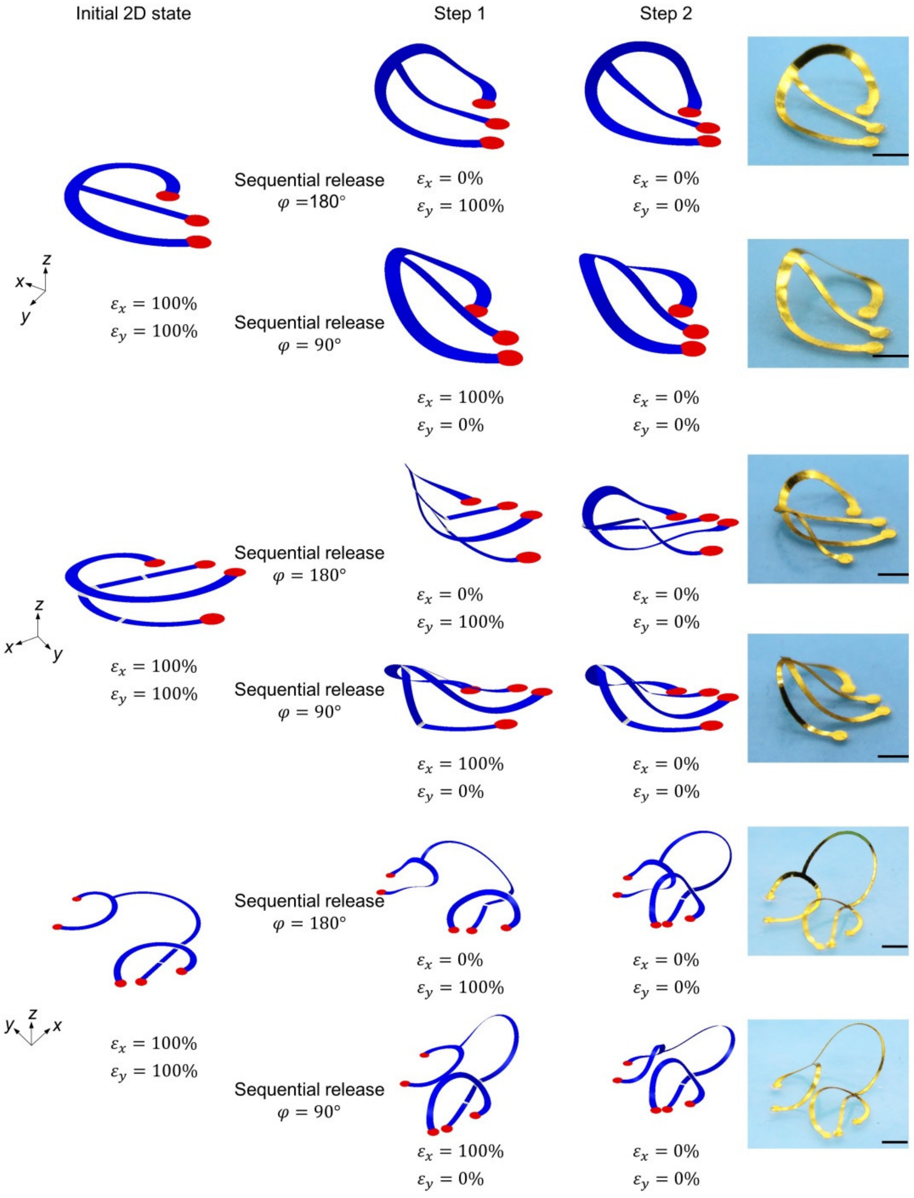

fig. S24. Additional examples of reconfigurable 3D mesostructures and the associated deformation sequences along different release paths. Photo Credit: Ke Bai, Tsinghua University.

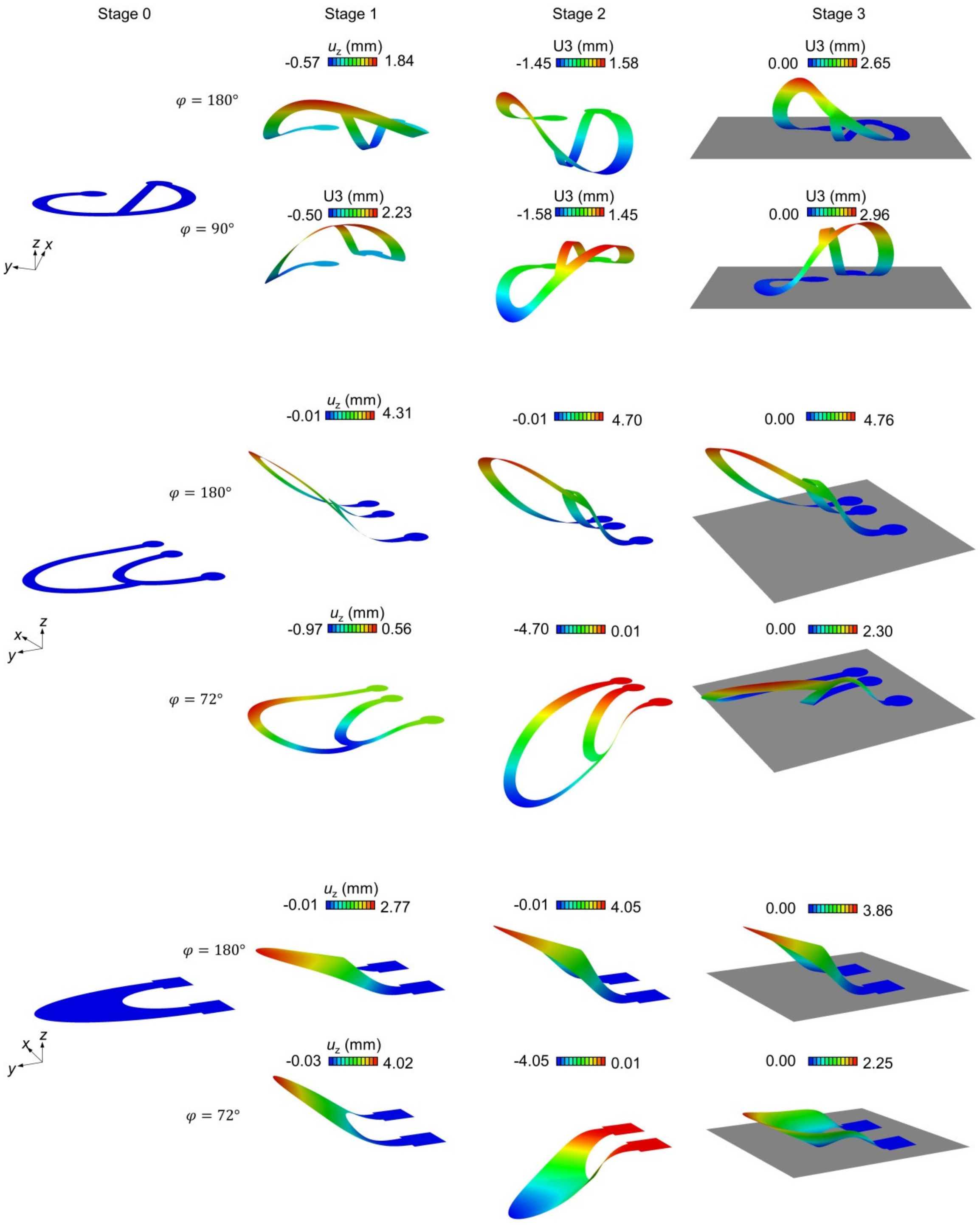

fig. S25. Illustration of the physical mechanism of symmetry break induced by the supporting substrate using three representative mesostructures in Fig. 3.

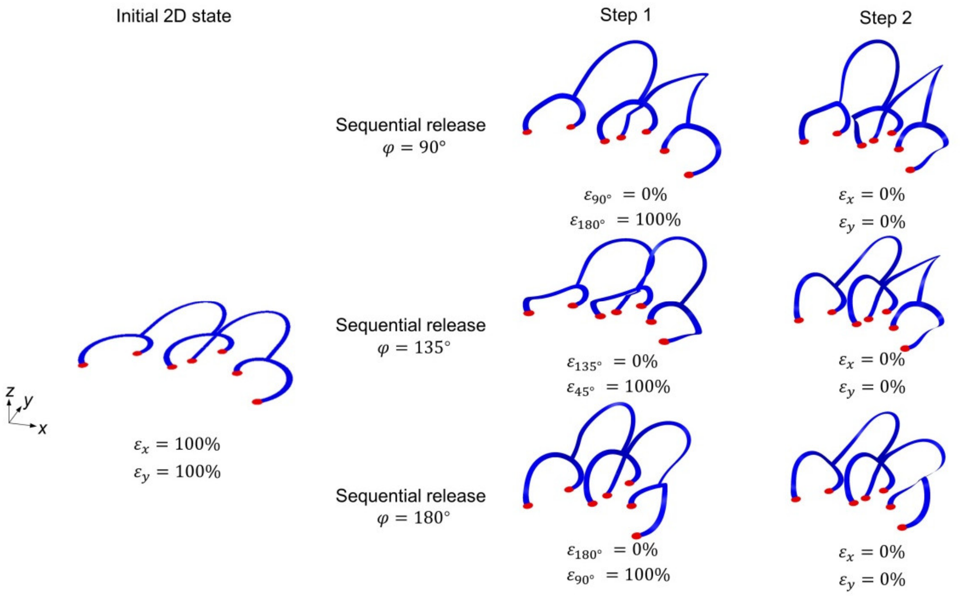

fig. S26. Deformation sequences for the first 3D mesostructure in Fig. 3E that offer three distinct stable configurations.

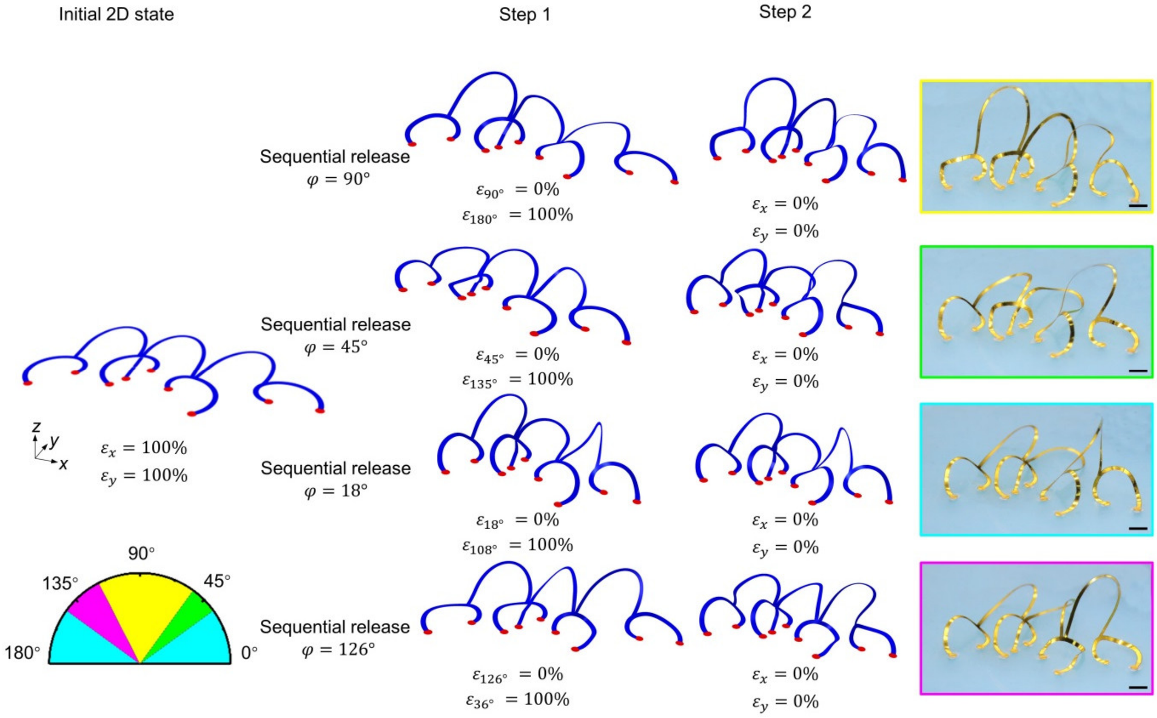

fig. S27. 2D precursor, phase diagram, deformation sequences and optical images for a ribbon-shaped 3D mesostructure with four distinct stable configurations. Photo Credit: Ke Bai, Tsinghua University.

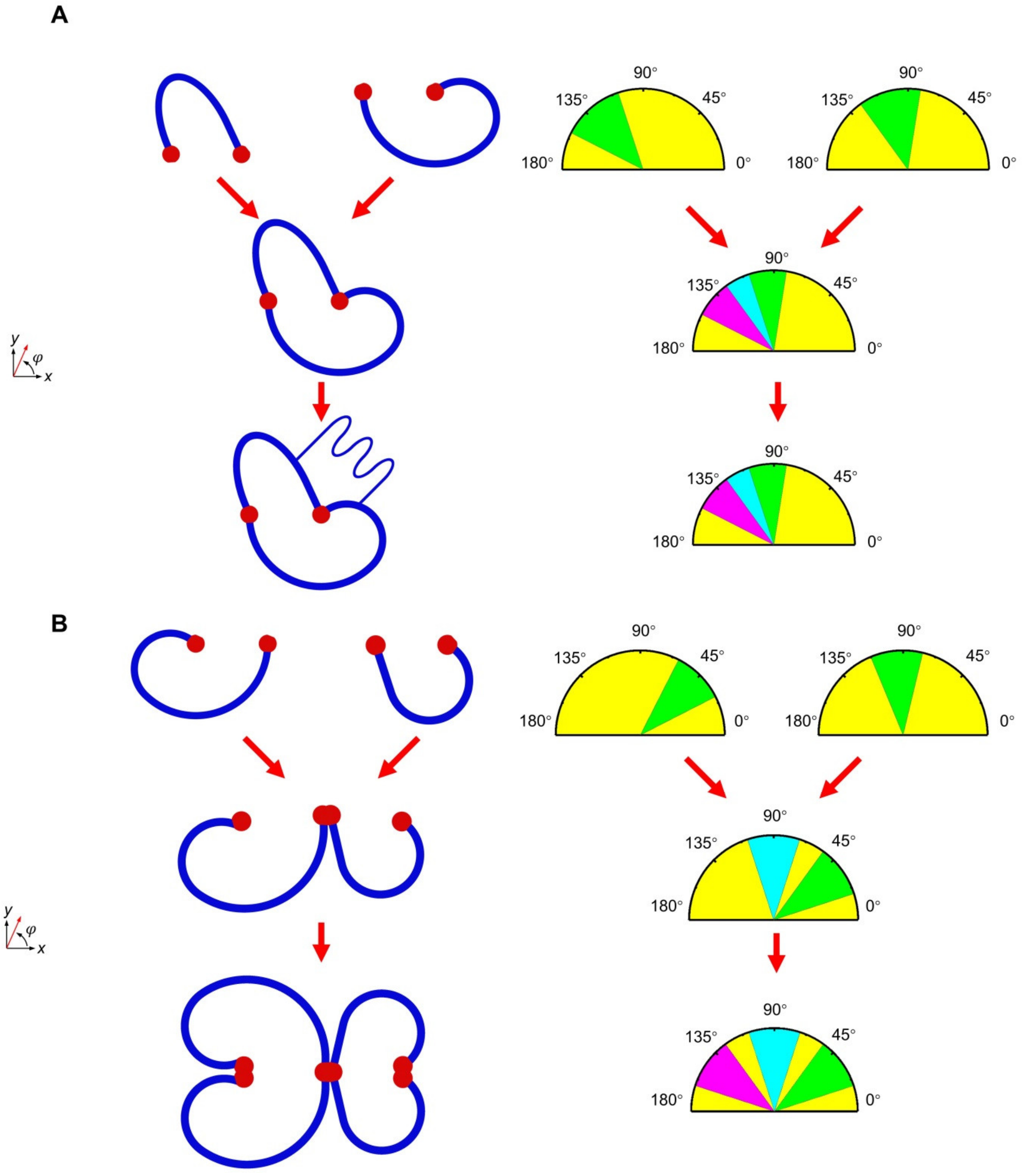

fig. S28. Illustration of the bottom-up strategy to build multimodal reconfigurable mesostructures by combining two (A) or four (B) elementary reconfigurable mesostructures.

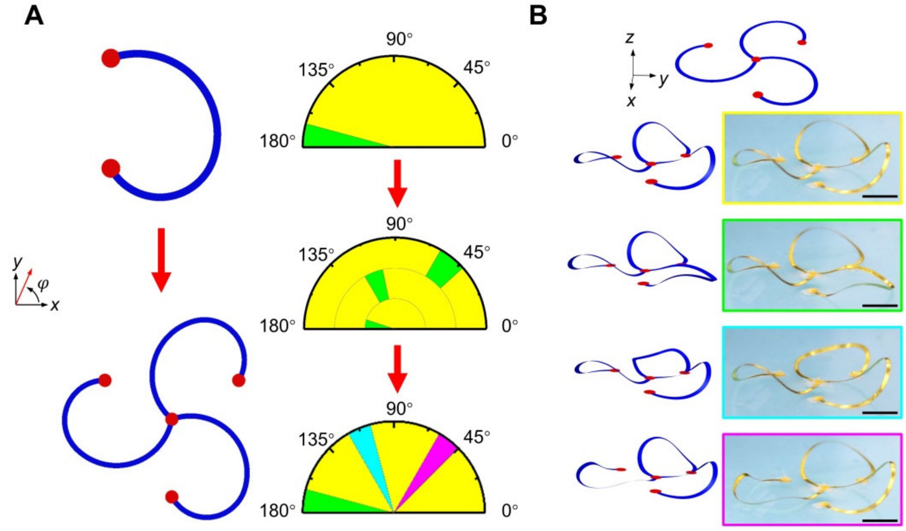

fig. S29. Illustration of the bottom-up strategy to build multimodal reconfigurable mesostructures by patterning elementary reconfigurable mesostructures in a circular array. Photo Credit: Ke Bai, Tsinghua University.

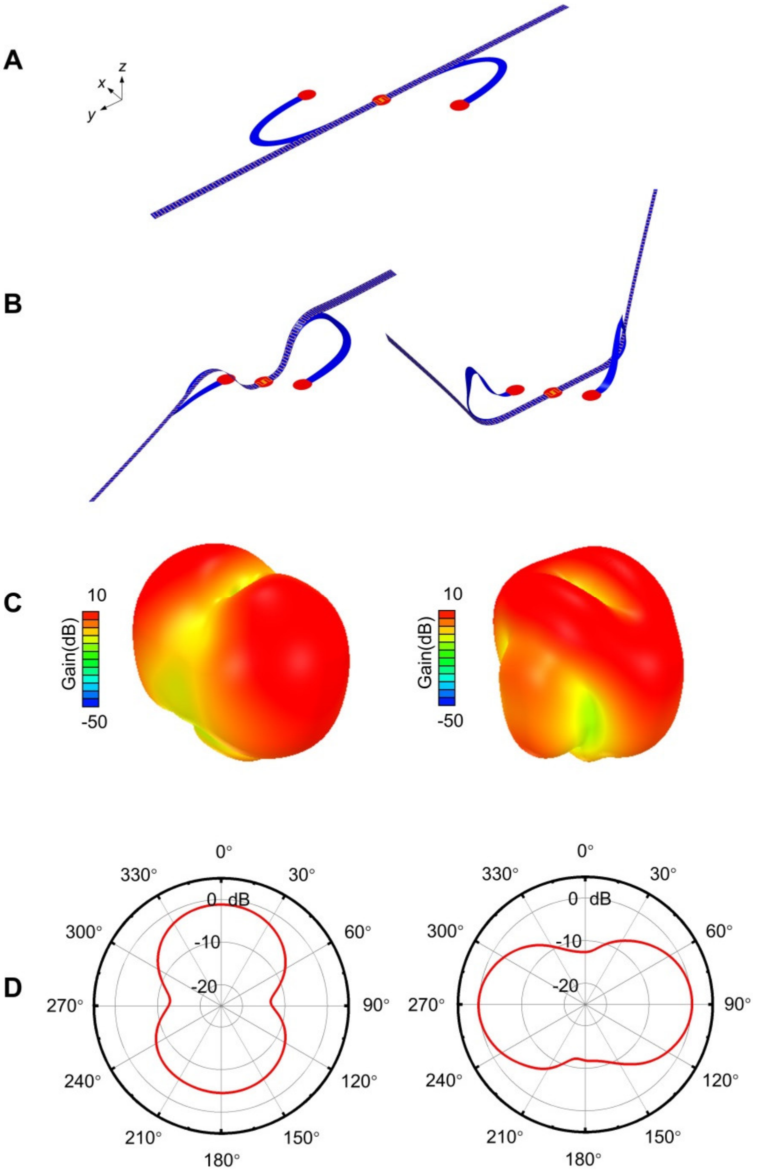

fig. S30. Results of electromagnetic simulation for a bi-stable whip antenna. (A), 2D precursor of a bi-stable whip antenna. **(B),** Two different modes of the bi-stable whip antenna. **(C),** 3D Gain surface of two different modes of the bi-stable whip antenna. **(D),** 2D Gain map on the H surface of two different modes of the bi-stable whip antenna.

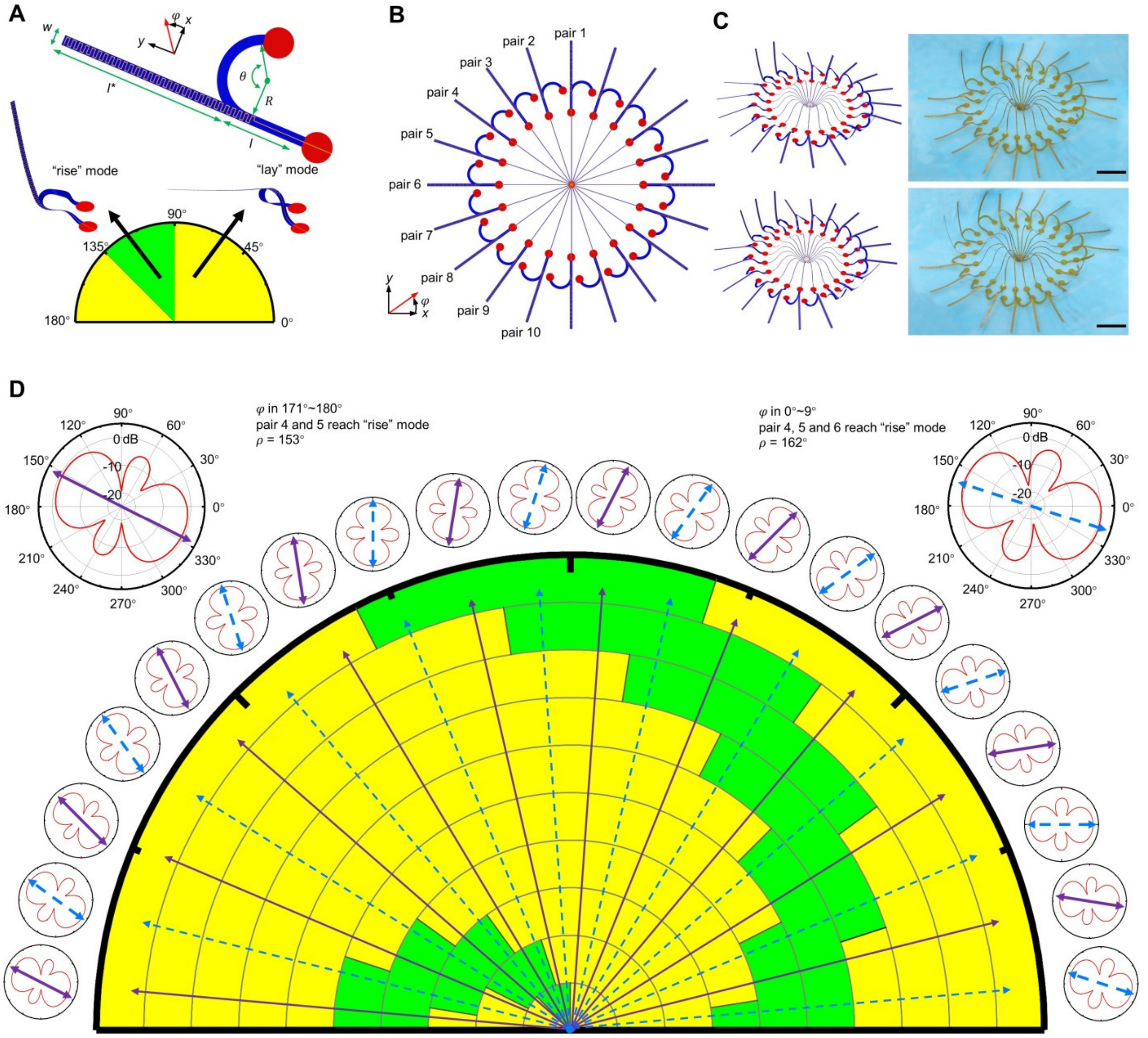

fig. S31. Design and results for a beam scanning antenna. (A), 2D precursor and phase diagram of a ribbon-shaped reconfigurable component of the beam scanning antenna, with the yellow, blue and red colours denoting the metallic layer (Cu, 6 μm), supporting layer (PI, 25 μm) and bonding sites, respectively. **(B-C)** 2D precursor, FEA results and optical images of a beam scanning antenna consisting of 10 pairs of reconfigurable components in (A)**. (D),** Phase diagram of the entire antenna that consists of 10 pairs of reconfigurable components, with the corresponding radiation patterns (simulated). Scale bars, 2 cm. Photo Credit: Ke Bai, Tsinghua University.

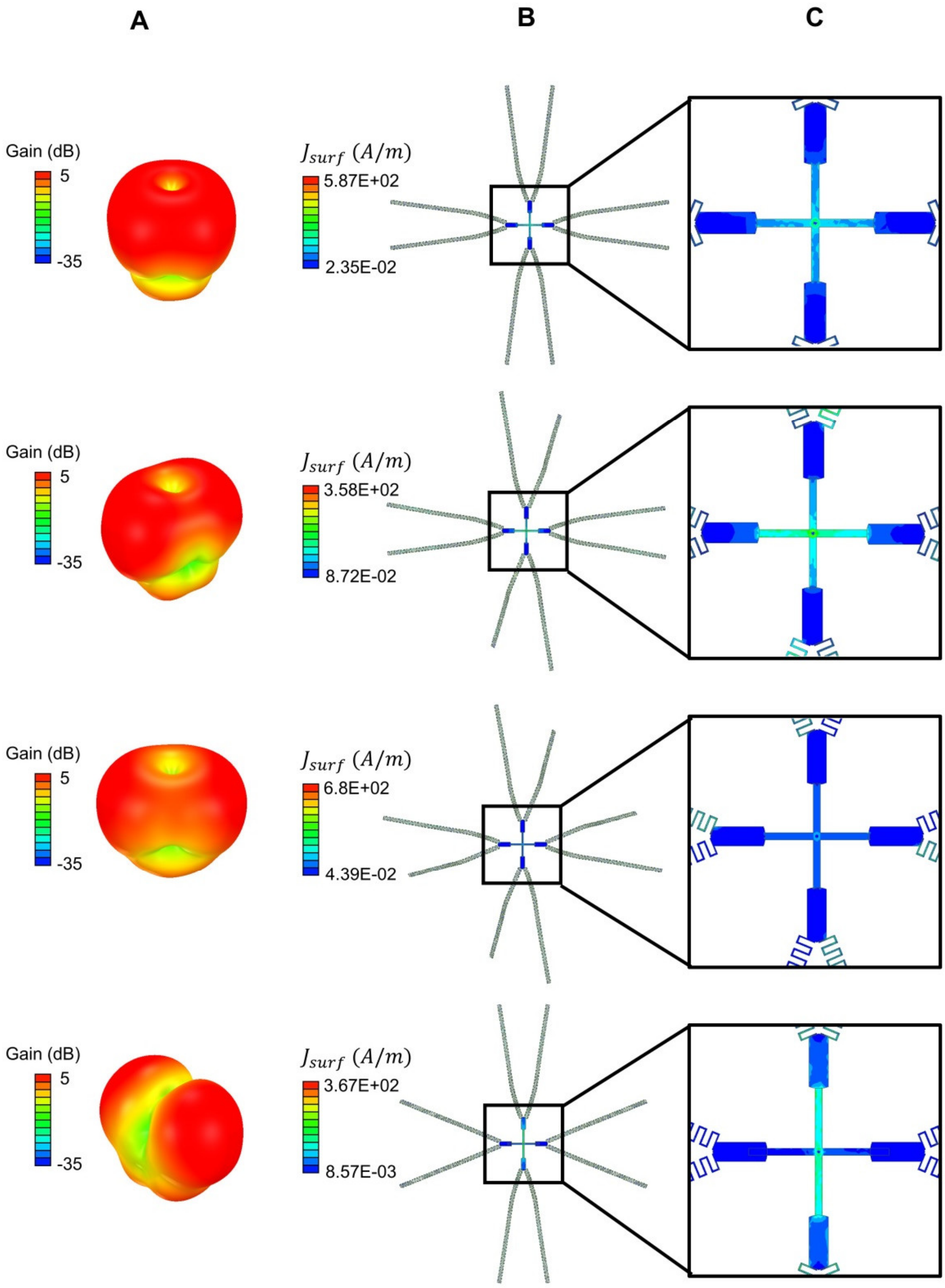

fig. S32. 3D radiation patterns and surface current distributions in the multimodal reconfigurable antenna at four different operation modes. (A), 3D radiation patterns of the multimodal reconfigurable antenna at four different operation modes discussed in Fig. 4I. **(B-C),** Surface current distributions in the whole antenna (B) and central region (C) at four different operation modes (top view).

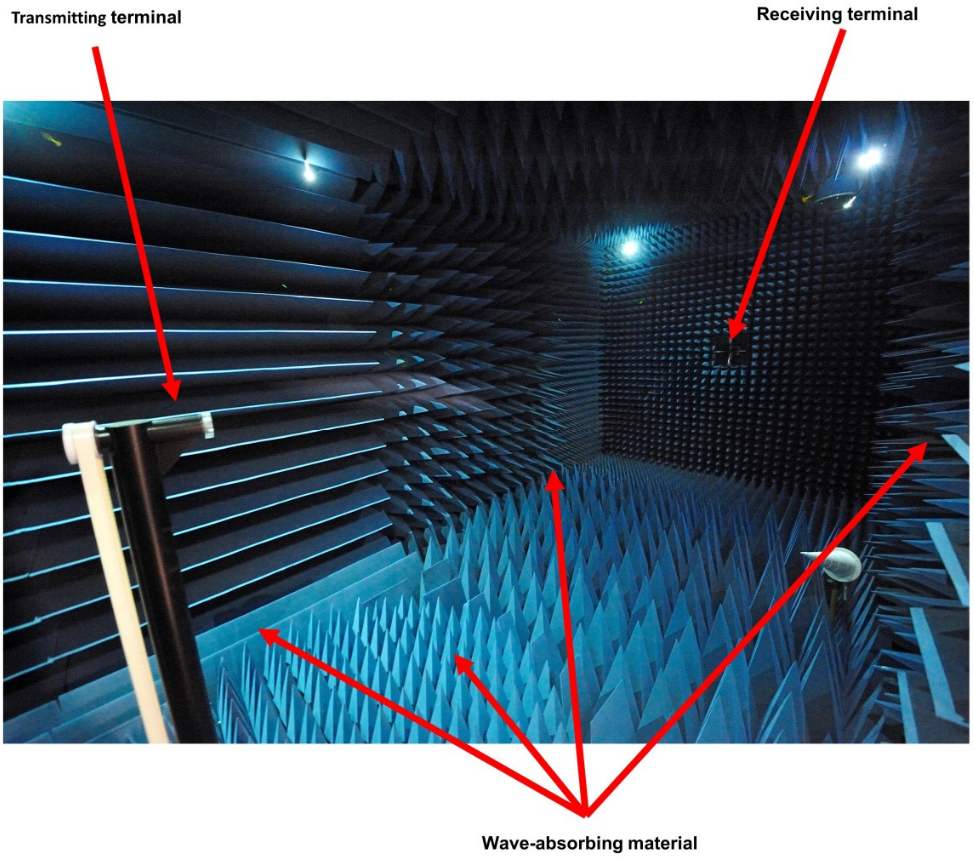

fig. S33. Experiment environment for measuring the antenna's radiation pattern. Device version: AMS8500. Scale: 8 m × 4 m × 4 m. Frequency range: 800 MHz ~ 18 GHz. Shielding performance ≥ 90 dB (6 GHz ~ 18 GHz). Homogeneity properties = ± 1 dB (axial direction), ± 0.5 dB (horizontal direction). Photo Credit: Lin Xiong, Tsinghua University.

Caption of Movies

Movie S1. A reconfigurable coil antenna array that can be switched to display the letters "T", "H" and "U" sequentially. Each antenna in the array consists of PI supporting layer, metallic layer, capacitor, and LED, and the on/off states can be switched through the 3D configuration controlled by the sequential loading scheme, based on a pre-stretched elastomer substrate. A planar primary coil attached onto the bottom surface of the substrate serves for energy transmission. Following the sequential release paths with three different angles (90°, 45° and 180° in the first step), the 3×3 array displays the letters "T", "H" and "U", respectively.

Movie S2. A reconfigurable mesostructure in Fig. 3B that can be reshaped between two different 3D configurations. Here, the mesostructure consists of a bilayer of aluminum (1 μm) and PI (25 μm). The left panel of the video displays the experimental measurement of the dynamic reconfiguration process of the mesostructure achieved by two different release paths. The right panel illustrates the corresponding FEA results.

Movie S3. A reconfigurable mesostructure in Fig. 3B that can be reshaped between two different 3D configurations. Here, the mesostructure consists of a bilayer of aluminum (1 μm) and PI (25 μm). The left panel of the video displays the experimental measurement of the dynamic reconfiguration process of the mesostructure achieved by two different release paths. The right panel illustrates the corresponding FEA results.

Movie S4. A reconfigurable mesostructure in Fig. 3E that can be reshaped among four different 3D configurations. Here, the mesostructure consists of a bilayer of aluminum (1 μm) and PI (25 μm). The left panel of the video displays the experimental measurement of the dynamic reconfiguration process of the mesostructure achieved by four different release paths. The right panel illustrates the corresponding FEA results.